Contents lists available at ScienceDirect

Arabian Journal of Chemistry

journal homepage: www.ksu.edu.sa

Synthesis and characterization of zinc stannate decorated on graphitic carbon nitride and study its potential for degradation of Eriochrome Black T and erythrosine under simulated sunlight

Masoumeh Hosseini [a], Mojgan Ghanbari [a], Elmuez A. Dawi [b], Usama S. Altimari [c], Aseel M. Aljeboree [d], Masoud Salavati-Niasari [a,*]

[a] Institute of Nano Science and Nano Technology, University of Kashan, Kashan, P. O. Box. 87317-51167, Iran
[b] College of Humanities and Sciences, Department of Mathematics, and Science, Ajman University, P.O. Box 346, Ajman, United Arab Emirates
[c] Department of Medical Engineering, Al-Nisour University College, Baghdad, Iraq
[d] Department of Chemistry, College of Science for Women, University of Babylon, Hilla, Iraq

ARTICLE INFO

Keywords:
$ZnSnO_3$/g-C_3N_4 Nanocomposite
Water purification
Photocatalytic Performance
Kinetics
Nanostructures

ABSTRACT

A key strategy for facilitating effective long-term photoinduced carrier separation and improving the photocatalytic efficiency of single photocatalysts is the development of heterojunction photocatalysts. The present study reports the fabrication of zinc stannate ($ZnSnO_3$, ZSO) using an effortless and inexpensive sonochemical approach, and zinc stannate/graphitic carbon nitride ($ZnSnO_3$/g-C_3N_4, ZSO/CN) nanocomposites with various contents of ZSO using a co-precipitation process assisted by ultrasound. Different instruments, including XRD, FTIR, FESEM, EDS, TEM, DRS, PL, BET, were used to characterize the purity, morphology, and structures of the products. The DRS data revealed that the introduction of CN reduced the bandgap of ZSO, which made it suitable for working in the visible region. The proficiency of ZSO, CN, and diverse ZSO/CN nanocomposites was perused for erythrosine (ER) and eriochrome black T (EBT) degradation. This is the first time ZSO/CN nanocomposites have been used to degrade organic dyes. The outcomes demonstrated that multiple elements impacted proficiency, for example, the amount of ZSO, quantity of catalyst, and concentration of dye. ZSO/CN nanocomposite containing 0.1 g ZSO showed the highest proficiency, in that 89.8 % of ER was degraded in the presence of 70 mg of ZSO/CN (0.1:1). The scavenger trials unveiled that superoxide radicals exhibited outstanding characteristics in the photoreactions. The kinetics survey manifested that a superior proficiency (89.8 %) donated the maximum rate constant (k = 0.0248 min^{-1}).

1. Introduction

One of the most promising approaches to address environmental pollution and energy issues is semiconductor-based photocatalysis because of its unmatched advantages (great proficiency, zero contamination, quick reaction rate, etc.) (Fang et al., 2023, Wang et al., 2023). Due to their non-toxicity, low-cost, high photosensitivity, and simple fabrication, inorganic semiconductors have received much concentration up until this point (Yao et al., 2016, Guo et al., 2019, Wen et al., 2022, Guo et al., 2023). As a notable versatile material, zinc stannate ($ZnSnO_3$, ZSO) has been used in a variety of disciplines, including gas sensors and photo-electrochemical devices (Qi and Sun 2016, Dong et al., 2020, Wang et al., 2022). The study of ZSO applications has slowly started to show interest in the field of photocatalysis in recent years (Beshkar et al., 2017). Smaller particle sizes can promote photocatalytic performance since photocatalyst size is connected to their photocatalytic action. As a result, numerous researchers created a range of ZSO nanostructures, particularly ZSO nanoparticles, to increase their photocatalytic efficacy (Huang et al., 2012). However, the use of pure ZSO in the field of photocatalysis is still severely constrained due to its high recombination of photo-induced carriers and low visible light harvesting performance (Eg = 3.23 eV) (Lo et al., 2015). Besides, during the photocatalytic reaction process, nanoparticles have a propensity to aggregate, which lowers stability (Liu et al., 2016, Yin et al., 2020). As a

Peer review under responsibility of King Saud University.
* Corresponding author.
E-mail address: Salavati@kashanu.ac.ir (M. Salavati-Niasari).

https://doi.org/10.1016/j.arabjc.2023.105395
Received 22 May 2023; Accepted 25 October 2023
Available online 28 October 2023

result, it is crucial to find a technique that may not only raise the separation rate of the photoinduced carriers and broaden the visible-light absorption area of ZSO but also enhance the dispersibility of ZSO NPs. One of the most common ways to successfully widen the light absorption spectrum and separate photo-induced electron-hole pairs in semiconductor photocatalysts is to design a heterojunction photocatalyst with two distinct semiconductors (Shi et al., 2019). The following fundamental criteria should be encountered when selecting a suitable semiconductor to couple with wide bandgap ZSO NPs: For enhanced visible light response, (i) two-dimensional (2D) mats are needed for nanoparticle dispersion; (ii) ZSO must have the suitable energy levels to match it in order to prevent photoinduced electron-hole pairs from recombining; and (iii) a narrow bandgap semiconductor is needed. Graphitic carbon nitride (g-C_3N_4, CN), an encouraging visible-light-driven photocatalyst, has received significant scientific attention and has been broadly used in the photocatalytic sector due to distinctive 2D layered structure, high chemical stability, and relatively narrow bandgap (Spataru et al., 2018, Zheng et al., 2018, Xie et al., 2022). For the photocatalytic process, various heterojunctions combined with CN have been described thus far (Liu et al., 2014, Tang et al., 2023). Certainly, CN can match well with ZSO (E_{CB} ~ -0.11 eV, E_{VB} ~ 3.12 eV) with appropriate band edges (E_{CB} ~ -1.3 eV, E_{VB} ~ 1.4 eV) (Arif et al., 2019), increasing the likelihood that the ZSO/CN heterojunction is formed. Electrons and holes generated by light can collect on the CB of ZSO and the VB of CN, respectively, which can separate the carriers generated by light. In addition, CN can be used as a dispersing substrate for nanoparticles (Liu et al., 2014, Mushtaq et al., 2021). Based on the overhead study, CN's multiple benefits make it a viable choice for combining with ZSO to boost its photocatalytic activity. Nevertheless, no prior research has been published using ZSO/CN heterojunction photocatalyst to degrade toxic dyes. The ZSO/CN heterojunction photocatalysts employed in this work were fabricated using a facile sonochemical-assisted co-precipitation approach. Below visible-light, the photocatalytic performance of the ZSO/CN heterojunctions was evaluated using organic dyes, including Eriochrome Black T (EBT) and Erythrosine (ER). The outcomes showed that the inclusion of the 2D CN nanosheets not only worked as a substrate to spread the ZSO NPs and constrain the aggregation of ZSO NPs but also increased the separation of the photoinduced ZSO carriers and light absorption. Degrading EBT and ER under visible radiation was used to determine the photocatalytic capabilities of ZSO/CN heterojunctions.

2. Methodology

2.1. Materials

Zinc nitrate hexahydrate 98 % $Zn(NO_3)_2{\cdot}6H_2O$, Stannic Chloride Pentahydrate 98 % $SnCl_4{\cdot}5H_2O$, Tetraethylenepentamine > 95 % (TEPA), Melamine 99.9 % ($C_3H_6N_6$), Ethylenediaminetetraacetic acid (EDTA), Erythrosine (ER), Benzoic acid (BA), Eriochrome Black-T (EBT), and 1,4-Benzoquinone (BQ), were obtained from Sigma-Aldrich and utilized with no more purification.

2.2. Procurement of ZSO

302 mg of $SnCl_4$ and 256 mg of $Zn(NO_3)_2$ were severally dissolved in 20 mL of distilled water and mixed for 15 min. The Zn^{2+} solution was added to the Sn^{4+} solution and mixed for 0.5 h. The combination was then exposed to an ultrasonic instrument for 10 min. TEPA was added to the mixture during the ultrasonic process till the solution pH reached 10. After centrifuging, the precipitate was dried for a day. The powder was ultimately calcined for 6 h at 750 °C (Scheme 1).

2.3. Preparation of ZSO/CN nanocomposites

The process began with the preparation of CN nanosheets, as previously discussed in our studies (Orooji et al., 2020, Ghanbari and Salavati-Niasari 2021). In a usual technique, a precise amount of melamine (7.0 g) was directly heated for 4 h at 550 °C. CN yellow powder was gathered for additional experiments. After that, 0.5 g of CN was dispersed using ultrasonic waves in 30 mL of distilled water for 50 min. The suspension containing CN was then added four times, in separate additions of 0.05, 0.15, 0.25, and 0.35 g of ZSO, and agitated for 24 h. The deposition was centrifuged and dried at 60 °C for a day. Scheme 2 depicts the schematic diagram of preparation of ZSO/CN nanocomposites.

2.4. Photocatalytic operation

The photocatalytic action of ZSO, CN, and ZSO/CN was affirmed via the decolorization of organic dyes, including EBT and erythrosine, below visible light radiation. 50 mg of ZSO, CN, and ZSO/CN were added into 50 mL of EBT and ER aqueous solutions and mixed for a half-

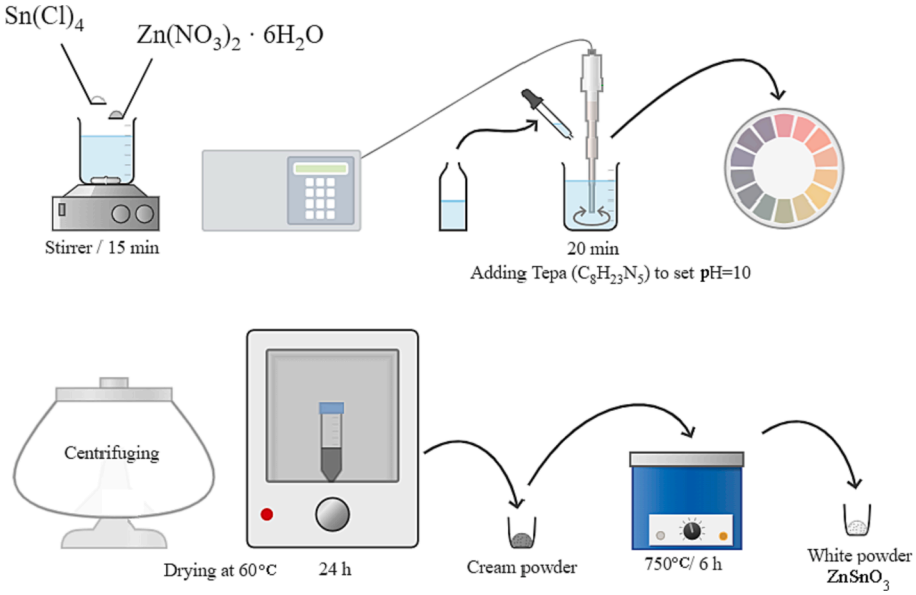

Scheme 1. Schematic diagram of preparation of ZSO structures.

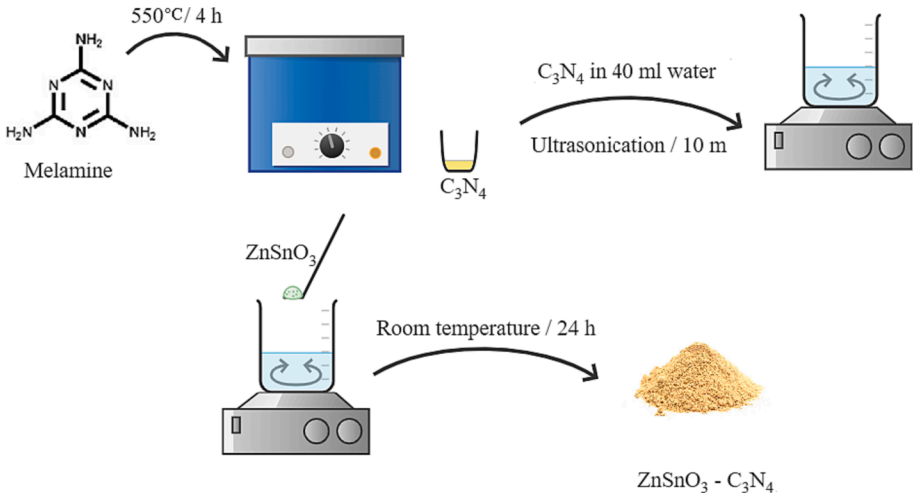

Scheme 2. Schematic diagram of preparation of ZSO/CN nanocomposites.

hour in the dark to reach an adsorption balance. A 400-watt Osram lamp was employed as the source of light to navigate the photocatalytic reaction. At particular gaps, 5 mL of the mixture was collected and scrutinized on a Vis spectrophotometer. During the catalysts' stability assessment, the employed photocatalysts were collected by centrifugation and filtering. Scavenger experiments confirmed the presence of active species. EDTA, BA, and BQ were utilized as scavengers to capture hole (h^+), hydroxide (•OH), and superoxide ($\bullet O_2^-$), respectively. The degradation percentage (%D) was calculated as follows:

$$D(\%) = \frac{A_0 - A_t}{A_0} \times 100 \quad (1)$$

The absorption of EBT or ER solutions at 0 and t time was symbolled as A_0 and A_t, respectively (Orooji et al., 2020).

3. Results and discussion

3.1. Characterization

The X-ray diffraction (XRD) pattern of CN is illustrated in Fig. 1a. This pattern matches well with 01–087-1526 C_3N_4 having hexagonal structures. CN has two unique peaks at 13.2° and 26.9°, which have been marked (0 0 1) and (0 0 2), respectively. Fig. 1b depicts the XRD pattern of pure $ZnSnO_3$, which shows 00–028–1486 zinc stannate with an orthorhombic crystal structure. Fig. 1(c-f) illustrates the XRD patterns of ZSO/CN nanocomposites with varying ZSO contents. $ZnSnO_3$ (00–028–1486) and carbon nitride (01–087-1526) form the peaks of these patterns. As the quantity of ZSO in the composition grows, so do the number and strength of ZSO peaks. The Scherrer equation (Tahir et al., 2020, Karami et al., 2021) was used to calculate the crystallite size, which was found to be in the 13.5 nm for CN and 27–34 nm for different ZSO/CN nanocomposites.

$$D = \frac{K\lambda}{\beta\cos\theta} \quad (2)$$

ZSO was synthesized using an ultrasound technique. Cavitation caused by ultrasonic waves is utilized to create appropriate structures. High energies are used to produce extremely high temperatures and pressures, which in turn make radicals that are active, according to the hot-spot theory (Dheyab et al., 2020). The following reactions demonstrate how the sonochemical approach is used to make the product: The sonochemical method is utilized to create the product, as shown by the reactions that follow:

$$H_2O \rightarrow \cdot OH + \cdot H \quad (3)$$

$$2\cdot OH \rightarrow H_2O_2 \quad (4)$$

$$2\cdot H \rightarrow H_2 \quad (5)$$

$$O_2 + \cdot H \rightarrow \cdot O_2H \quad (6)$$

$$\cdot O_2H + \cdot H \rightarrow H_2O_2 \quad (7)$$

$$\cdot O_2H + \cdot O_2H \rightarrow H_2O_2 + O_2 \quad (8)$$

$$H_2O + C_8H_{23}N_5 + \cdot H \rightarrow OH^- + C_8H_{23}N_5 - H^+ \quad (9)$$

$$Zn(NO_3)_2 + OH \rightarrow Zn(OH)_2 + NO_3^- \quad (10)$$

$$Sn^{4+} + Zn(OH)_2 \rightarrow ZnSnO_3 \quad (11)$$

Fig. 2 unveils Fourier-transform infrared (FTIR) spectra of CN, ZSO, and ZSO/CN nanocomposites. The FTIR spectrum of ZSO (Fig. 2a) exhibited multiple bands at 474, 619, 1120, 1404, and 1540 cm^{-1}. The infrared absorption spectrum of ZSO shows the vibrational frequency at 474 cm^{-1} indicates the presence of Zn–O and frequency band at around 619 cm^{-1} indicates the presence of Sn–O vibrations in ZSO. The absorption bands at 1120, 1404, and 1540 cm^{-1} are attributed to the tensile modes of M−O (Sn-O and Zn-O) (Huang et al., 2020, Ghanbari et al., 2022). The band at 1640 cm^{-1} and the wide one at 3424 cm^{-1} are imputed to bending and stretching vibrations of O–H absorbed on the ZSO surface, respectively (Ghanbari et al., 2021). Pure CN (Fig. 2b) shows the peaks for 1, 3, 5-triazine vibrations at 805 cm^{-1} and between 1242 and 1639 cm^{-1} for C-N and C = N vibrations, respectively. The stretching vibration of N–H of carbon nitride is also present 3175 cm^{-1}. The inclusion of ZSO did not alter the original structure of CN nanosheets (Fig. 2(c-f)).

The Field emission scanning electron microscopy (FESEM) was used to study the morphology of samples. The surface morphology of ZSO is indicated in Fig. 3a. Microstructures and, in some areas, nanoparticles are visible in Fig. 3a. Fig. 3b reveals the nanoflake morphology of pure CN. In-situ formation of ZSO on the surface of CN changes the size and morphology of ZSO. The FESEM image of ZSO/CN (0.1:1) is displayed in Fig. 3c. The nanoflakes are the dominant phase in the image due to the low content of ZSO. The ZSO nanoparticles with some agglomeration are formed on the CN surface (Fig. 3d) when the mass ratio of ZSO to CN is 0.3 to 1. Increasing the amount of ZSO to 0.5 caused irregularly nanoflakes (Fig. 3e). ZSO covers the surface of CN by enhancing the amount of ZSO to 0.7. The TEM photographs of ZSO/CN (0.1:1) are indicated in Fig. 4. ZSO nanoparticles are more obvious in these figures compared to the SEM image (Fig. 3c). The average particle size of the $ZnSnO_3$

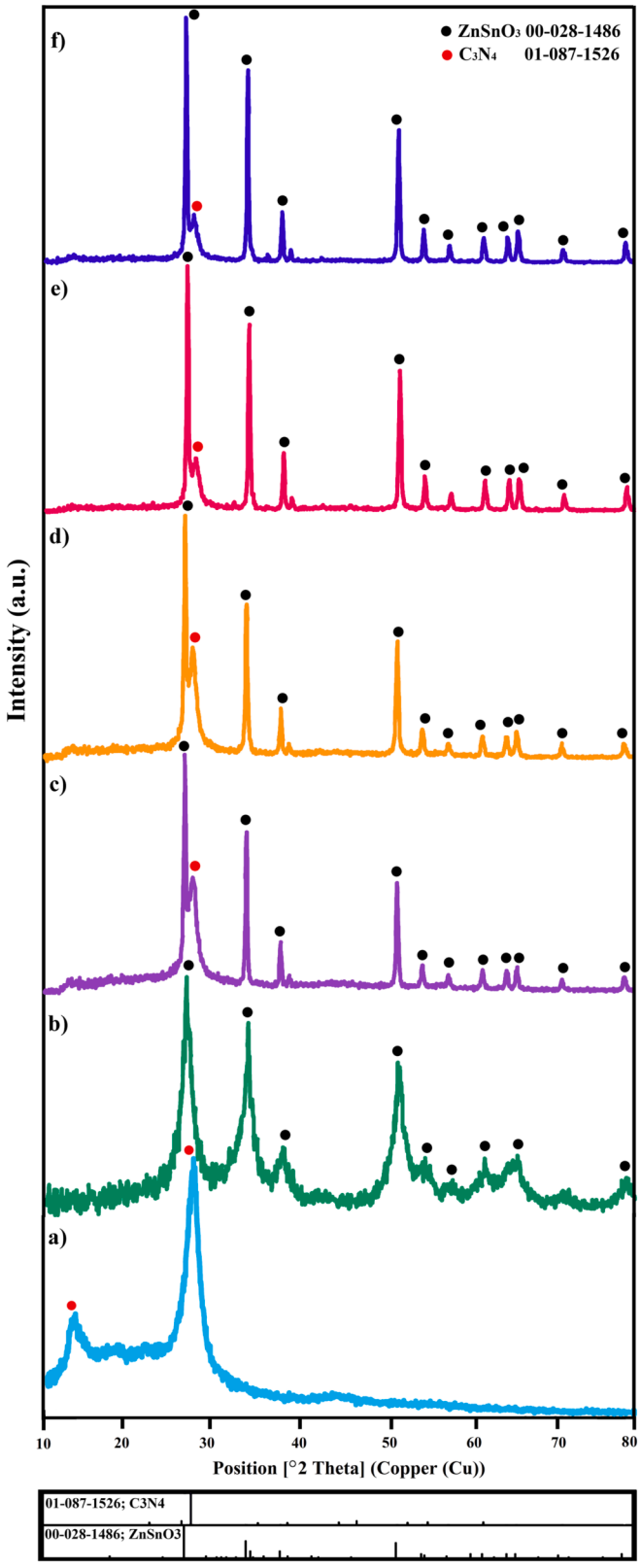

Fig. 1. The XRD patterns of a) CN, b) ZSO, c) ZSO/CN (0.1:1), d) ZSO/CN (0.3:1), e) ZSO/CN (0.5:1), and f) ZSO/CN (0.7:1).

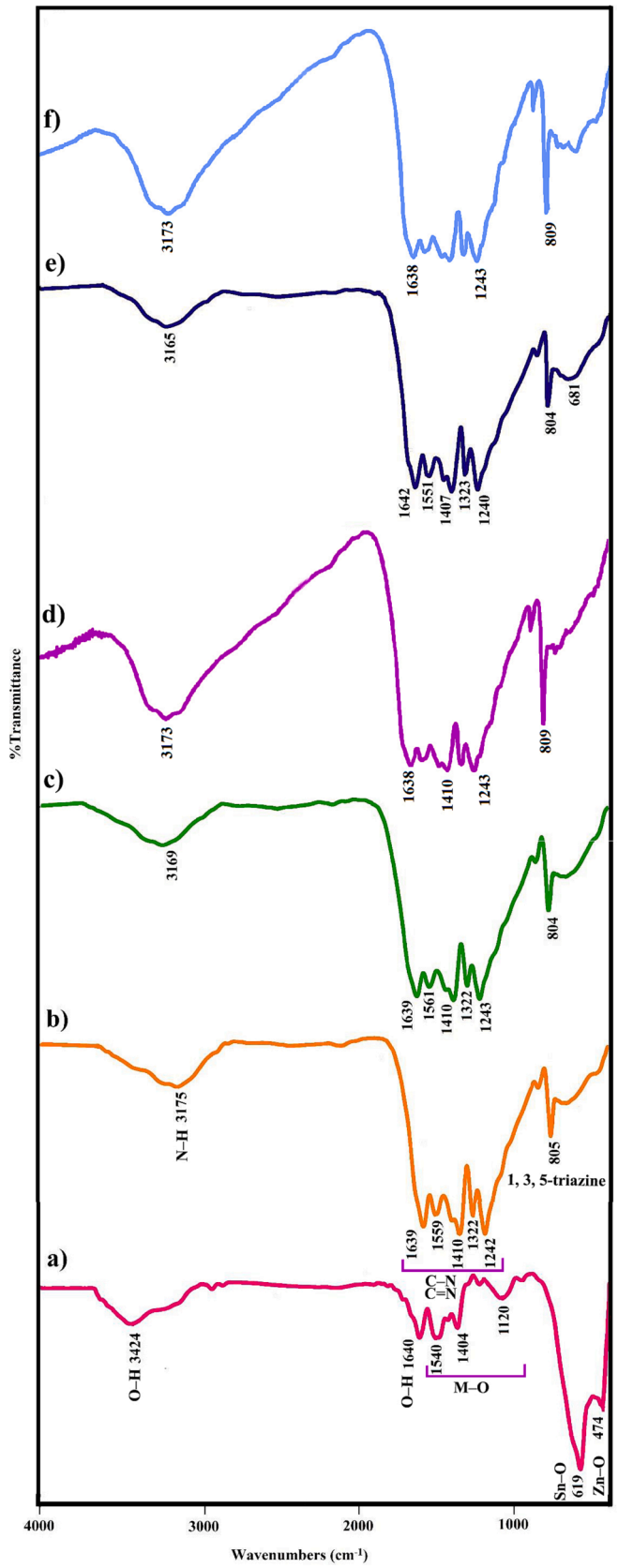

Fig. 2. The FTIR spectra of a) ZSO, b) CN, c) ZSO/CN (0.1:1), d) ZSO/CN (0.3:1), e) ZSO/CN (0.5:1), and f) ZSO/CN (0.7:1).

crystallites is estimated by Digimizer software to be 18 nm from the TEM image.

To further confirm the composition and purity of the samples, the electron dispersive X- ray spectroscopy (EDS) spectra of four different

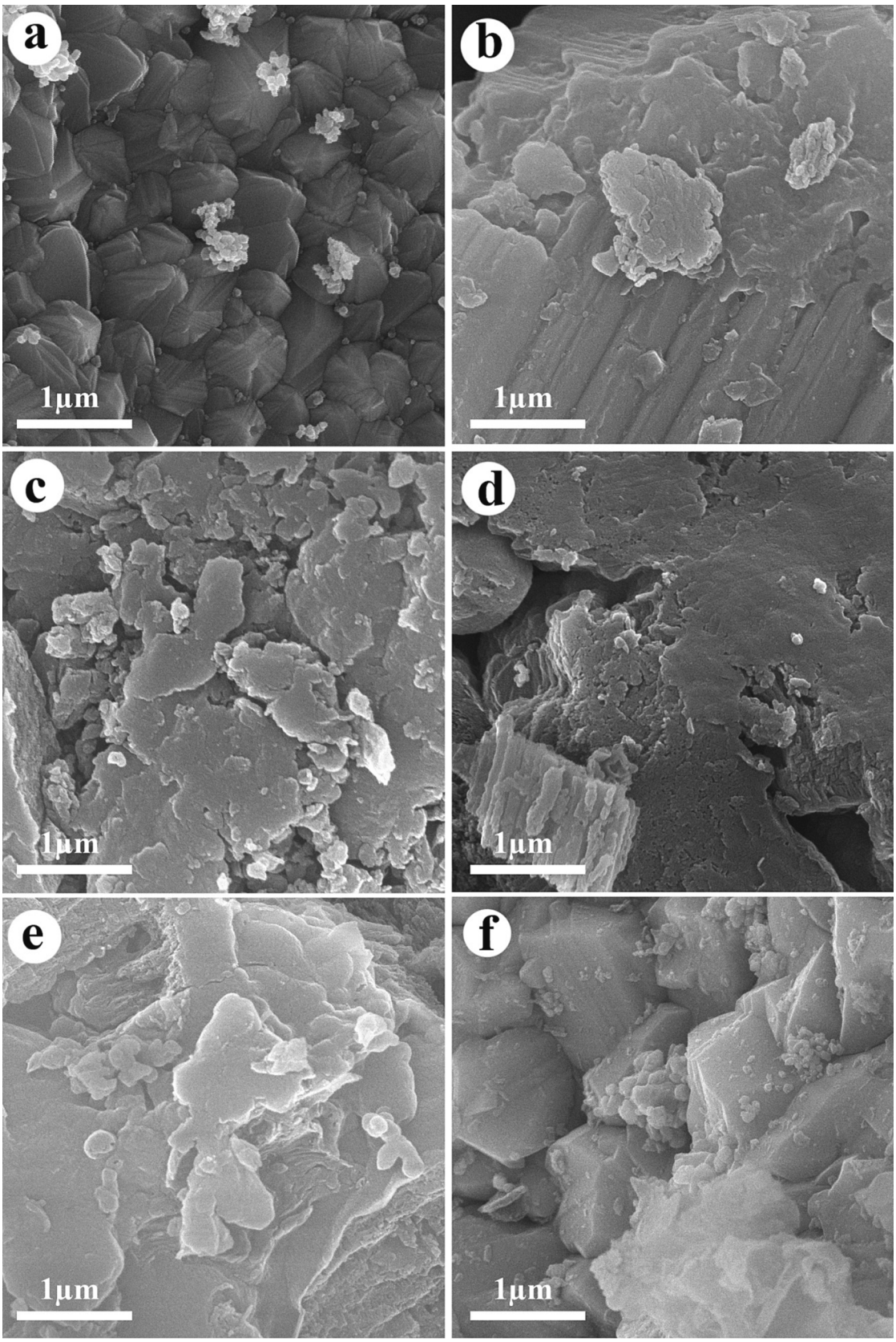

Fig. 3. FESEM images of a) ZSO, b) CN, c) ZSO/CN (0.1:1), d) ZSO/CN (0.3:1), e) ZSO/CN (0.5:1), and f) ZSO/CN (0.7:1).

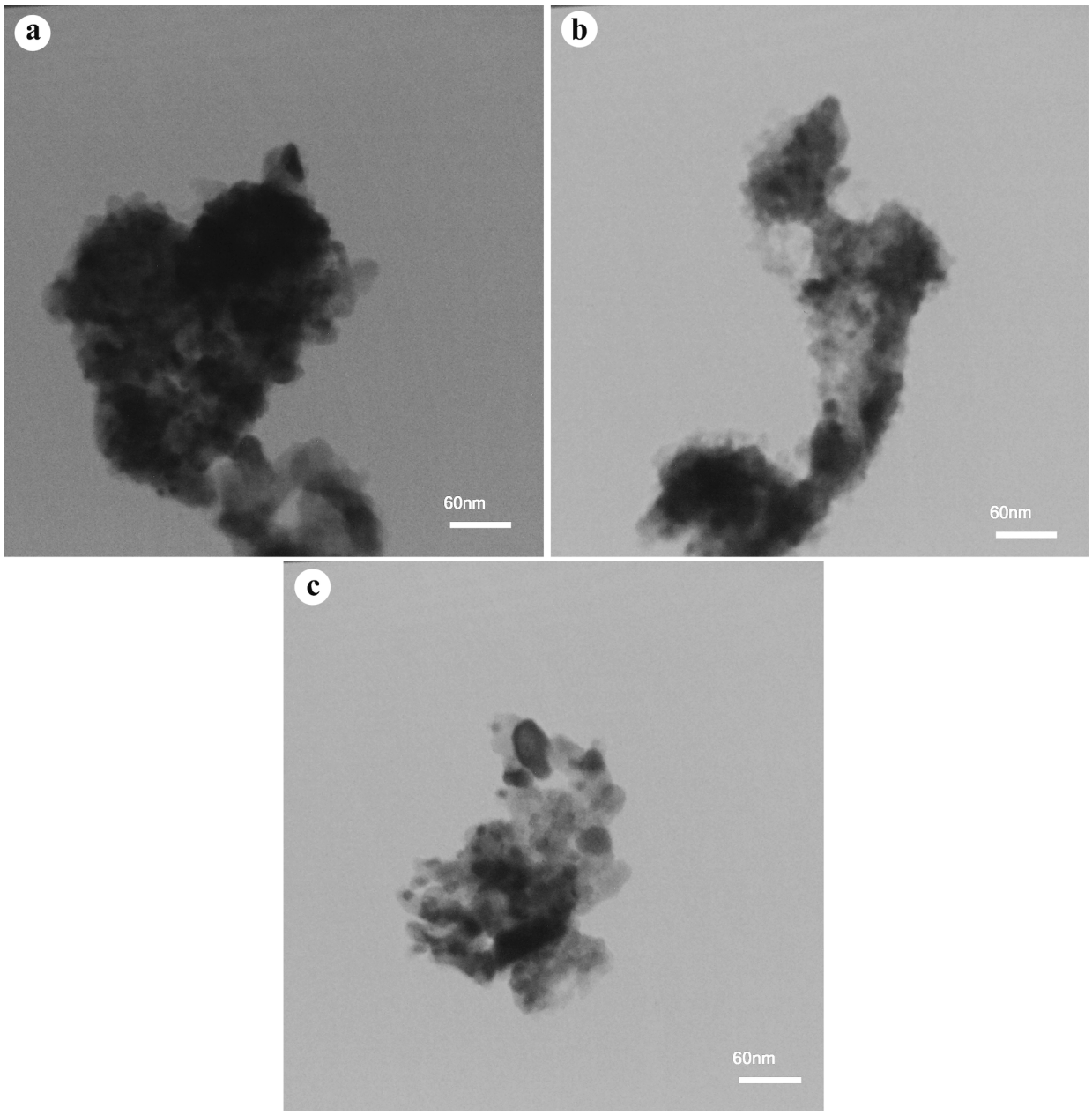

Fig. 4. TEM images of ZSO/CN (0.1:1) nanocomposites.

nanocomposites are depicted in Fig. 5(a-d). The presence of elements, such as Zn, O, Sn, C, and N in these spectra provides strong evidence for the successful synthesis of ZSO/CN nanocomposites. The inclusion of carbon and nitrogen indicates that carbon nitride (CN) is indeed present in these nanocomposites.

Fig. 6a pictures the N_2 isotherms and pore size distribution plots of CSO/CN (0.1:1). The isotherm fits with the IV-type isotherm and H3 hysteresis. The BET plot gives the specific surface area at 5.599 m^2/g, total pore volumes at 0.010028 cm^3/g, and mean pore diameters at 7.163 nm. The BJH plot displays that the size distribution of nanoparticles is in the range of 1–10 nm (Fig. 6b).

The absorption edge, or optical absorption, is often connected to the electrical excitation from the VB to the CB. As a consequence, the subject sample's optical bandgap energy can be calculated utilizing the DRS information. The Kubelka-Maunk (K-M) formula and the accompanying Tauc graphs are the most efficient means of accomplishing this goal. The following relation must be employed in a typical K-M equation, to convert absolute R-values (in%) to K-values, a measure of the converted R (Panahi et al., 2023).

$$K = (1 - R)^2/2R \tag{12}$$

Then, the bandgap of sample can be determined by the Tauc equation:

$$(\alpha h\upsilon) = \beta(h\upsilon - E_g) \tag{13}$$

In Eq. (13), υ is light frequency, $h = 6.626 \times 10^{-34}$ J s denote Planck constant. α is the absorption coefficient that counts on the sample thickness (d) and the absorbance (A) of sample, α= ([2.303 × A]/d). β associates with the sample absorbance. The power "n" contains a variable value depending on the type of electronic transition. Hence, it takes values of 2 and 3 for the allowed and forbidden indirect transitions, while it takes 1/2 and 3/2 for the allowed and forbidden direct transitions, respectively (Panahi et al., 2023). The band gap value of ZSO was estimated at 3.23 eV, as seen in Fig. 6c. ZSO/CN (0.1:1) nanocomposites show bandgap values at 2.7 eV for both CN and ZSO (Fig. 6d). The

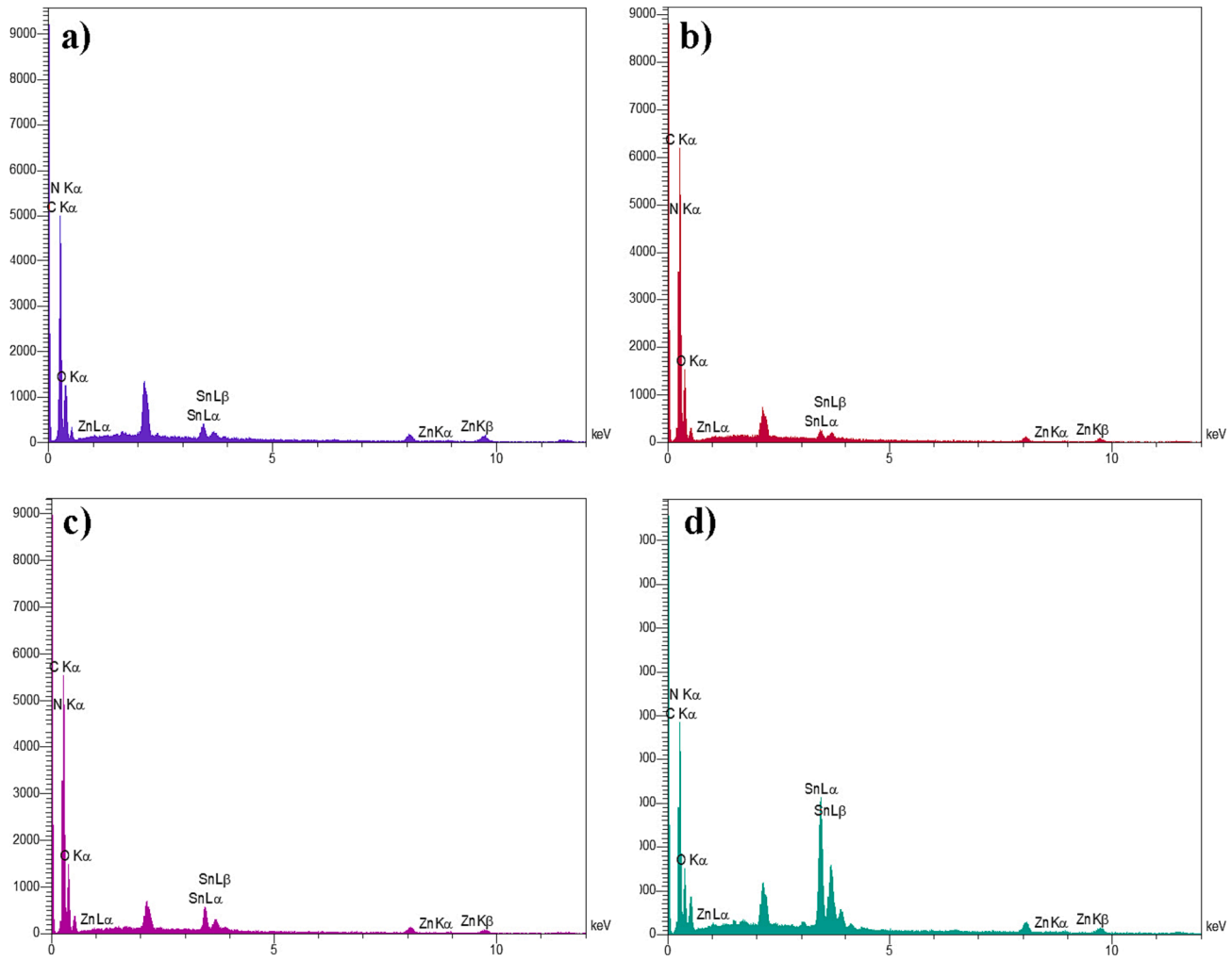

Fig. 5. EDS spectra of a) ZSO/CN (0.1:1), b) ZSO/CN (0.3:1), c) ZSO/CN (0.5:1), and d) ZSO/CN (0.7:1).

introduction of CN reduced the bandgap of ZSO, which made it suitable for working in the visible region.

The charge carrier separation characteristics of pure CN, ZSO, and ZSO/CN (0.1:1) nanocomposite were studied by photoluminescence (PL) spectroscopy. It is generally agreed that the semiconductor material with lower PL intensity means high photoinduced electron-hole pairs separation efficiency (Guo et al., 2021). Fig. 6e reveals the strong emission signals of all as-prepared material at around the wavelength of 425–500 nm. Compared with pure phases, the PL strengths of ZSO/CN (0.1:1) nanocomposite is obviously reduced, indicating that charge carriers have higher separation efficiency in the binary photocatalytic system.

3.2. Catalyst photoactivity

Different types of catalysts, including CN, ZSO, and ZSO/CN with various content of ZSO, were applied to degrade EBT and ER under visible light. It is crucial study several factors, such as ZSO content, organic dyes, catalyst content, and concentration of dye, for improvment the photocatalytic performance. Fig. 7a manifests the presence of different types of catalyst on the degradation of EBT. As seen, 51.1 % and 40.2 % of EBT were degraded in the presence of pure CN and ZSO, respectively. Addition 0.1 g ZSO to CN boosts the EBT degradation to 80.5 % (ZSO (0.1): CN (1.0)) under visible radiation. The more increasing in the content of ZSO caused the reduction of efficiency. So that, 76.1 % and 72.4 % of EBT were degraded in the presence of 0.3 g and 0.5 g of ZSO, respectively. Nevertheless, 68.0 % of EBT was degraded in the presence of 0.7 g ZSO, which is much greater than pristine ZSO and CN. Fig. 7b reveals the efficiency of different catalysts on the degradation of ER. The general trend of the results is similar to the degradation of EBT, with the difference that the percentage of degradation is slightly increased in all samples. So that, 56.1 %, 52.6 % of ER were degraded in the presence of pure CN and ZSO, respectively. 83.7 %, 78.1 %, 75.4 %, and 70.5 % of ER were degraded in the presence of different content of ZSO. It can be inferred that the combination of ZSO with CN boosts the performance and further degrades organic dyes (EBT or ER). One of the influential elements for boosting the efficiency of the photocatalytic reaction is the amount of catalyst. Fig. 7c portrays the degradation of ER in the presence of different amounts of ZSO/CN (0.1:1) nanocomposites. As the catalyst content increases, the efficiency improves. 70, 50, and 30 mg of ZSO/CN (0.1:1) nanocomposite can degrade 89.8 %, 83.7 %, and 70.7 % of ER, respectively. Three concentrations of ER, including 5, 10, and 15 ppm, were studied over ZSO/CN (0.1:1). As seen in Fig. 7e, 89.8 %, 78.7 %, and 67.1 % of 5, 10, and 15 ppm ER were degraded. The results show that enhancing ER concentration results in reduction of efficiency. Langmuir-Hinshelwood mechanism was applied to estimate the reaction rate (Baladi et al., 2020):

$$\ln(\frac{C_0}{C}) = kt \tag{14}$$

C_0 is ER concentration at t_0 and C is ER concentration at t. The pseudo rate constant (k) was derived using $\ln(C_0/C)$ linear correlations

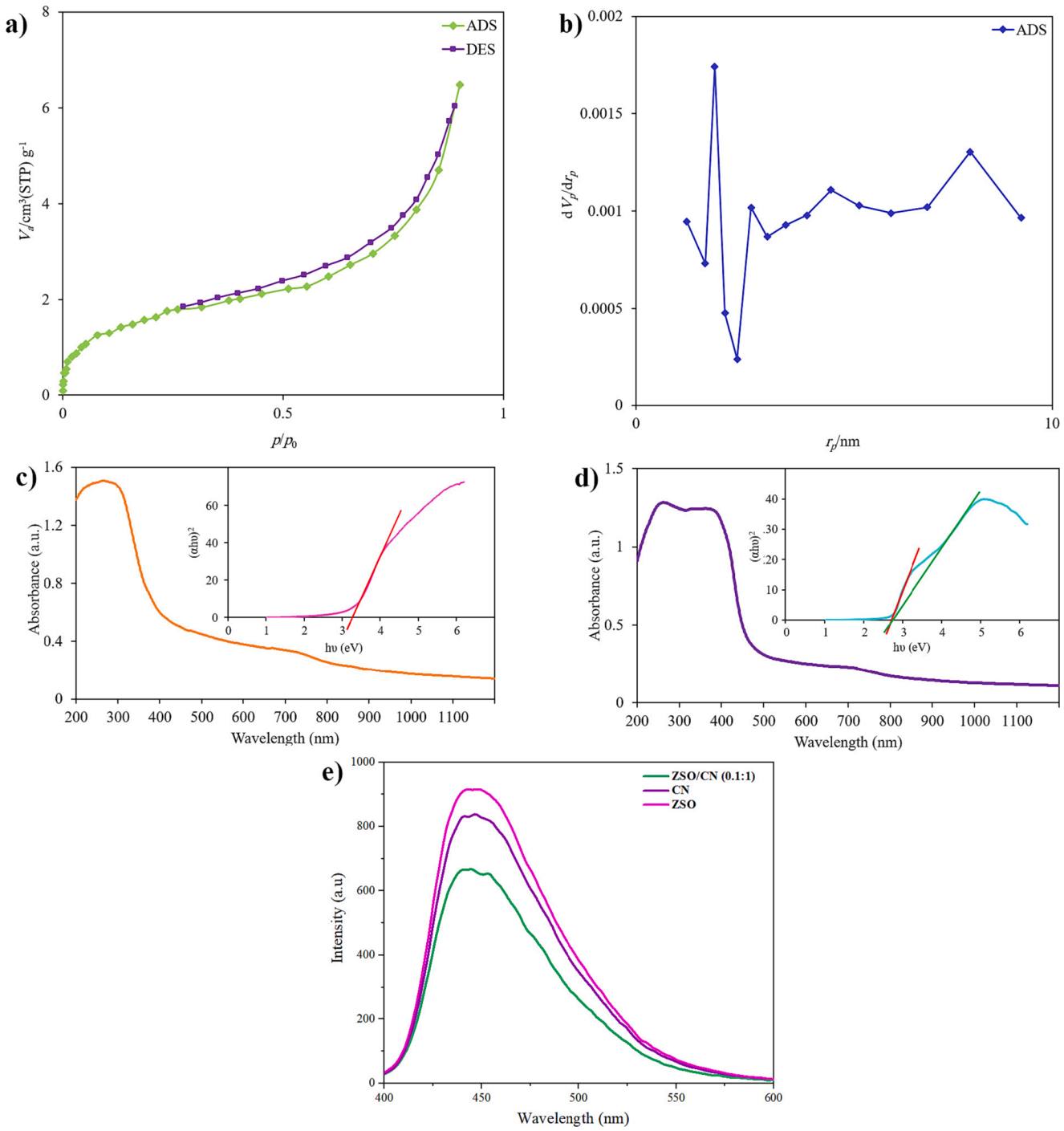

Fig. 6. a) n_2 isotherm, b) BJH plot of ZSO/CN (0.1:1), DRS spectra and Tauc plots of c) ZSO, d) ZSO/CN (0.1:1) and e) photoluminescence emission spectra of pure ZSO, CN and ZSO/CN (0.25:1).

vs. time. The best photocatalytic effectiveness was reached by utilizing a higher rate coefficient, as shown in Fig. 7d and 7f. The influence of various parameters on photocatalytic performance is depicted in Fig. 7, which demonstrates that the highest rate coefficient was required to produce the best photocatalytic performance.

Scavenger experiments utilizing BA, EDTA, and BQ to quench •OH, h^+, and $\bullet O_2^-$, respectively, were performed in order to demonstrate the function of active species in ER degradation (Rahimzade et al., 2021). Adding BQ to the mixture, as shown in Fig. 8a, caused the rate of photocatalytic degradation to drop from 83.9 % to 37.1 %, proving that $\bullet O_2^-$ is the most common active species in photocatalytic reactions. The photocatalytic efficiency of the combination reduced when BA and EDTA were added separately, going from 83.9 % to 82.9 % and 73.1 %, respectively, showing that the effects of •OH and h^+ on the deterioration of ER were insignificant (Sakthivel et al., 2003). When oxygen molecules are present, the electron (e^-) reaction can form active oxygen ($\bullet O_2^-$), which can react in a number of various manners (Wenderich and Mul 2016).

The valence band (VB) and conduction band (CB) potential of a semiconductor can be theoretically calculated using Mulliken electronegativity and the bandgap of a semicconductor by the following formulas (Cheng et al., 2019):

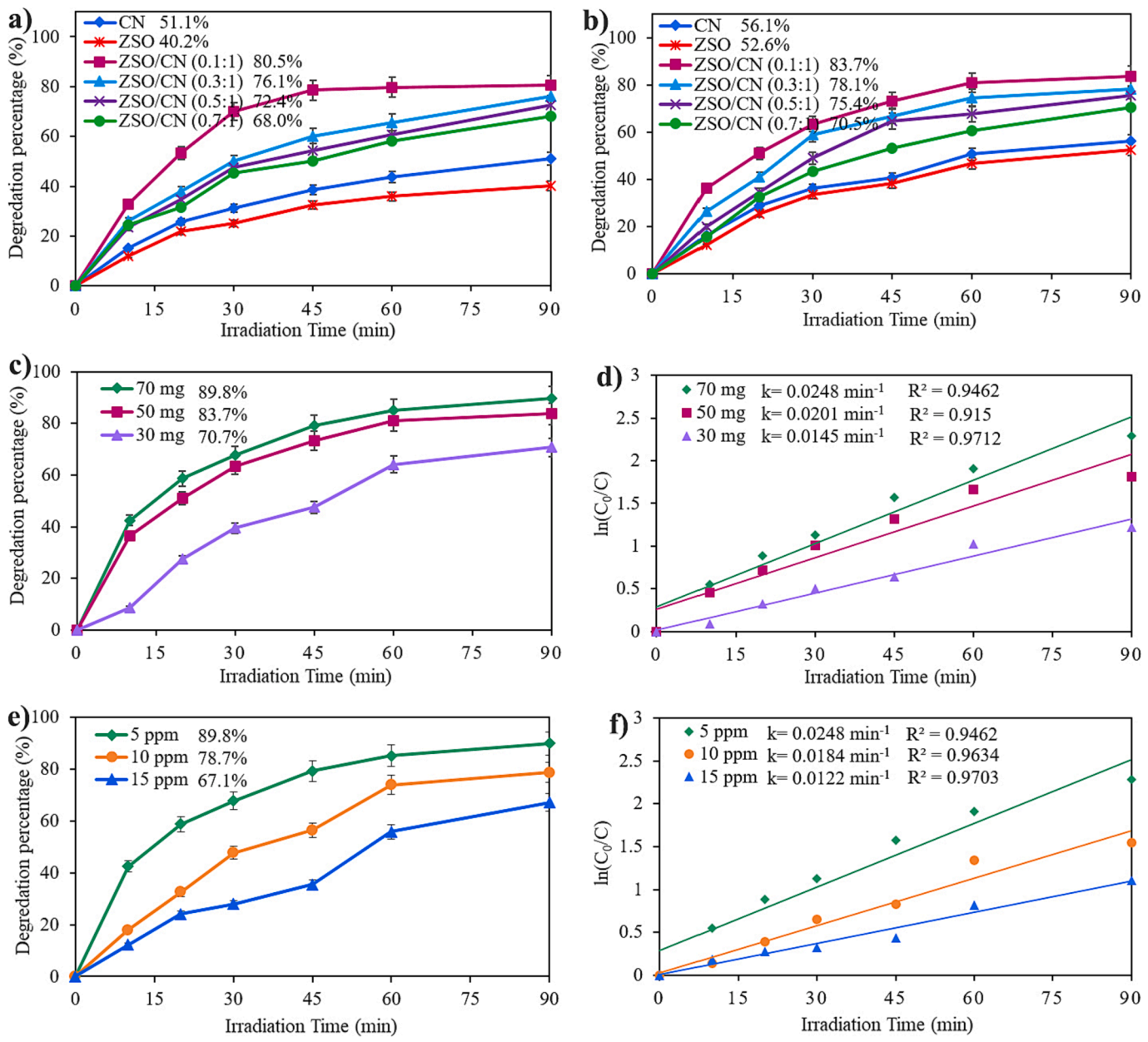

Fig. 7. Photodegradation of a) EBT, b) ER in the prsence of ZSO, CN, and different ZSO/CN nnocomoposites, c) effect of different dosages, d) $\ln(C_0/C)$ vs. time of ZSO/CN (0.1:1), e) effect of different concentration of ER and f) $\ln(C_0/C)$ vs. time in the presence of ZSO/CN (0.1:1).

$$E_{VB} = X - E_e + 0.5E_g \quad (15)$$

$$E_{CB} = E_{VB} - E_g \quad (16)$$

where E_{VB} and E_{CB} are the top of the valence band and the bottom of the conduction band of the semiconductor, E_g is the band gap energy, E_e is the energy of free electrons on the hydrogen scale with a fixed value of 4.5 eV vs. NHE (Cheng et al., 2019), and X is the geometric mean of the Mulliken electronegativity of the constituent atoms in the semiconductor. The Mulliken electronegativity of an atom is the arithmatic mean of the first ionization energy and the first electron affinity. Therefore, VB and CB positions of ZSO were determined at 2.48 and −0.75 eV, respectively. In addition, VB and CB of pure CN were reported to be + 1.4 eV and − 1.3 eV, respectively (Paul et al., 2020).

Based on the above conclusions, the photocatalytic degradation mechanism of ER towards ZSO/CN composite was tentatively discussed. Under the illumination of visible light, the photoinduced electrons and holes is generated for the CN due to the relatively narrower band gap (2.7 eV). However, as for ZSO ($E_g \approx 3.23$ eV), it was hard to be excited to generate photoinduced carriers at the same conditions because of its wider bandgap. According to the matchable CB levels, the photo-excited electrons from CB of CN (-1.3 eV vs. NHE) could transfer to the CB of ZSO (-0.75 eV vs. NHE), and left the photo-excited holes on the VB of CN, thus facilitating the separation of the photogenerated electron-hole pairs. The CB of ZSO was more negative than $O_2/\bullet O_2^-$ (-0.046 eV vs. NHE) (Chen et al., 2016, Kumar and Rao 2017), photo-generated electrons on the CB of ZSO can capture O_2 to produce $\bullet O_2^-$, directly degrading ER. Owing to the VB of CN (1.4 eV vs NHE) was lower than $\bullet OH/OH^-$ (2.70 eV vs. NHE) (Wang et al., 2015), thereby the h^+ resided in the VB of CN directly oxidized ER through photocatalytic reaction. In the following, the reactions that occurred on the surface of the catalyst and drove to the ER decolorization are presented (Konstantinou and Albanis 2004, Safajou et al., 2021):

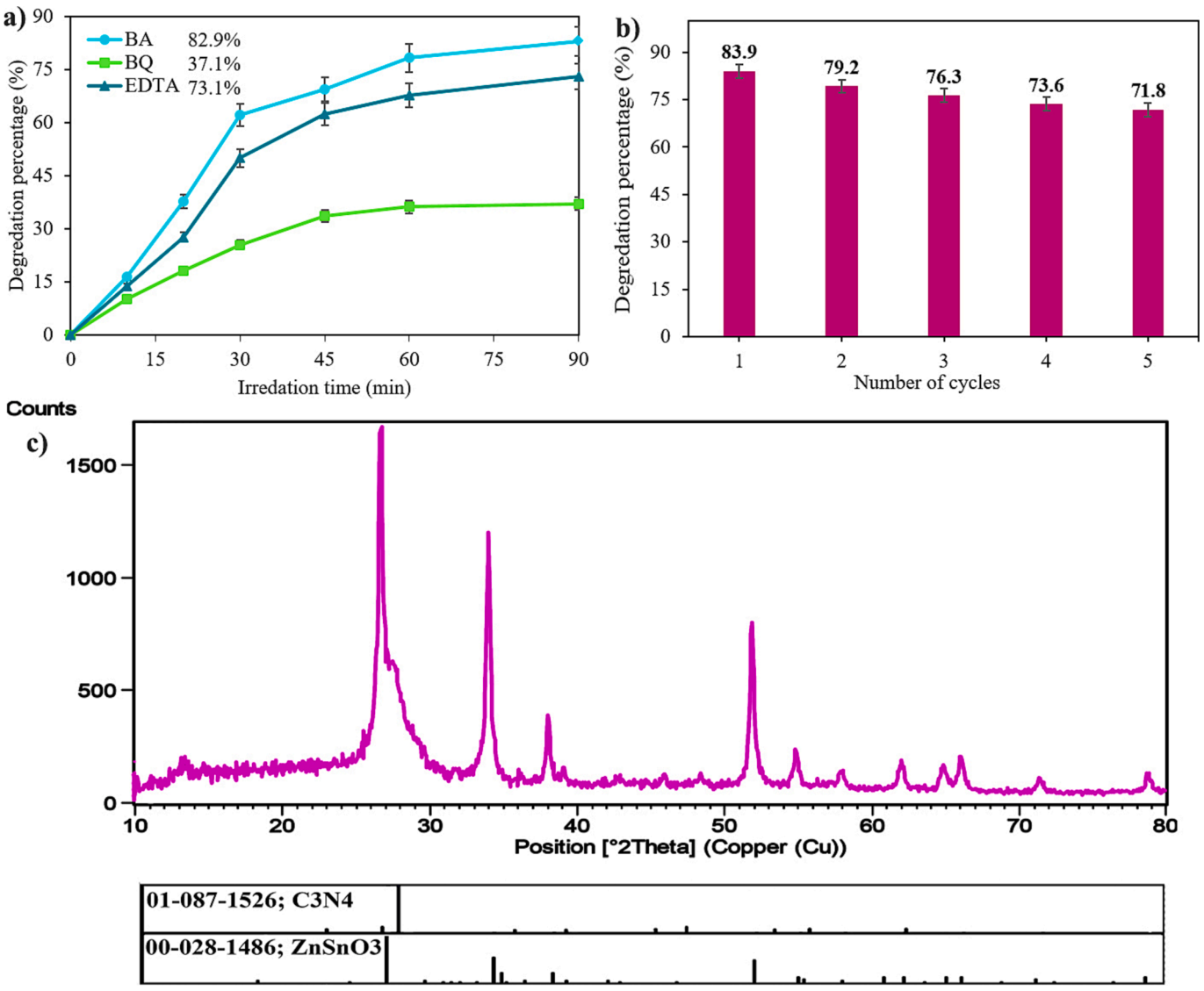

Fig. 8. a) effect of scavengers, b) recycle test, and c) xrd pattern of zso/cn (0.1:1) after recycling.

$$ZSO/CN + h\nu \rightarrow ZSO/CN(e_{CB}{}^{-} + h_{VB}{}^{+}) \quad (17)$$

$$CN(e^{-} + h^{+}) \rightarrow ZSO(e^{-}) + CN(h^{+}) \quad (18)$$

$$e^{-} + O_2 \rightarrow O_2{\cdot}^{-} \quad (19)$$

$$\cdot O_2{}^{-} + ER \rightarrow \mathrm{deg}radationproducts(e.g., CO_2, H_2O, H_2) \quad (20)$$

$$h^{+} + ER \rightarrow \mathrm{deg}radationproducts(e.g., CO_2, H_2O, H_2) \quad (21)$$

The reusability test was executed to dissect the stability of ZSO/CN (0.1:1). A typical technique involved centrifuging ZSO/CN, washing it with water, letting it dry overnight at 65 °C, and then using it five more times under the exact circumstances. ZSO/CN (0.1:1) is durable and maintains its possible proficiency for five cycles, as shown in Fig. 8b. After five cycles, the efficiency has decreased by 12.1 %. The decrease in efficiency after five cycles could be attributed to several factors. Loss of active sites during the centrifugation and washing process. Accumulation of impurities: Over multiple cycles, impurities from the reaction mixture or from the washing process may accumulate on the ZSO/CN material. These impurities can block or hinder the active sites, reducing the efficiency of the material. Structural degradation: The repeated use and exposure to high temperatures during drying can lead to structural degradation of the ZSO/CN material. This can result in a loss of stability and a decrease in efficiency over time. Surface fouling: The ZSO/CN material may undergo surface fouling due to adsorption of reaction by-products or other contaminants present in the reaction mixture. This fouling can reduce the accessibility of active sites and decrease efficiency. The XRD pattern for the reused ZSO/CN (0.1:1) is illustrated in Fig. 8c. All diffraction peaks are related to $ZnSnO_3$ (00–028–1486) and carbon nitride (01–087-1526). This pattern is in good agreement with the fresh ZSO/CN (0.1:1) before the photocatalytic reaction.

4. Conclusions

In overview, ZSO/CN nanocomposites with different contents of ZSO were fabricated by co-precipitation assisted by ultrasonic. The degradation of organic dyes, such as ER and EBT, was scanned in the presence of CN, ZSO, and ZSO/CN. In the perfect state, 70 mg of ZSO/CN (0.1:1) degraded 89.8 % of ER. These results confirmed that this compound had a grand prospect in water remedy usage. Superoxide radicals recreated the most role in photoreactions. This compound was seen to be stable in the reusable trial and only lost 12.1 % of its efficiency after five cycles.

CRediT authorship contribution statement

Masoumeh Hosseini: Software, Investigation, Methodology, Formal analysis. **Mojgan Ghanbari:** Formal analysis, Data curation, Investigation, Software. **Elmuez A. Dawi:** Conceptualization, Writing – review & editing, Software. **Usama S. Altimari:** Conceptualization, Writing – review & editing, Software. **Aseel M. Aljeboree:** Writing – review & editing, Software. **Masoud Salavati-Niasari:** Software, Formal analysis, Methodology, Writing – review & editing, Writing – original draft, Conceptualization, Supervision, Project administration, Investigation, Data curation, Validation, Resources, Visualization, Funding acquisition.

Declaration of Competing Interest

The authors declare that they have no known competing financial interests or personal relationships that could have appeared to influence the work reported in this paper.

Acknowledgements

The authors have delightedly appreciated the financial assistance of the University of Kashan(Grant No. 159271/MH2) and the council of Iran National Science Foundation (INSF, 97017837).

References

Arif, M., Yasin, G., Shakeel, M., et al., 2019. Hierarchical CoFe-layered double hydroxide and gC 3 N 4 heterostructures with enhanced bifunctional photo/electrocatalytic activity towards overall water splitting. Mater. Chem. Front. 3, 520–531.

Baladi, M., Ghanbari, M., Valian, M., et al., 2020. DyMnO 3/Fe 2 O 3 nanocomposites: simple sol-gel auto-combustion technique and photocatalytic performance for water treatment. Environ. Sci. Pollut. Res. 28, 11066–11076.

Beshkar, F., Amiri, O., Salehi, Z., 2017. Synthesis of ZnSnO3 nanostructures by using novel gelling agents and their application in degradation of textile dye. Sep. Purif. Technol. 184, 66–71. https://doi.org/10.1016/j.seppur.2017.04.024.

Chen, F., Yang, Q., Niu, C., et al., 2016. Enhanced visible light photocatalytic activity and mechanism of ZnSn (OH) 6 nanocubes modified with AgI nanoparticles. Catal. Commun. 73, 1–6.

Cheng, Y., He, L., Xia, G., et al., 2019. Nanostructured gC 3 N 4/AgI composites assembled by AgI nanoparticles-decorated gC 3 N 4 nanosheets for effective and mild photooxidation reaction. New J. Chem. 43, 14841–14852.

Dheyab, M.A., Aziz, A.A., Jameel, M.S., et al., 2020. Mechanisms of effective gold shell on Fe3O4 core nanoparticles formation using sonochemistry method. Ultrason. Sonochem. 64, 104865.

Dong, S., Cui, L., Zhang, W., et al., 2020. Double-shelled ZnSnO3 hollow cubes for efficient photocatalytic degradation of antibiotic wastewater. Chem. Eng. J. 384, 123279.

Fang, X., Tang, Y., Ma, Y.-J., et al., 2023. Ultralong-lived triplet excitons of room-temperature phosphorescent carbon dots located on g-C3N4 to boost photocatalysis. Sci. China Mater. 66, 664–671.

Ghanbari, M., Salavati-Niasari, M., Mohandes, F., 2021. Injectable hydrogels based on oxidized alginate-gelatin reinforced by carbon nitride quantum dots for tissue engineering. Int. J. Pharm. 602, 120660.

Ghanbari, M., Sadjadinia, A., Zahmatkesh, N., et al., 2022. Synthesis and investigation of physicochemical properties of alginate dialdehyde/gelatin/ZnO nanocomposites as injectable hydrogels. Polym. Test. 110, 107562.

Ghanbari, M., Salavati-Niasari, M., 2021. Copper iodide decorated graphitic carbon nitride sheets with enhanced visible-light response for photocatalytic organic pollutant removal and antibacterial activities. Ecotoxicol. Environ. Saf. 208, 111712 https://doi.org/10.1016/j.ecoenv.2020.111712.

Guo, F., Li, M., Ren, H., et al., 2019. Fabrication of p-n CuBi2O4/MoS2 heterojunction with nanosheets-on-microrods structure for enhanced photocatalytic activity towards tetracycline degradation. Appl. Surf. Sci. 491, 88–94. https://doi.org/10.1016/j.apsusc.2019.06.158.

Guo, F., Huang, X., Chen, Z., et al., 2021. Construction of Cu3P-ZnSnO3-g-C3N4 p-n-n heterojunction with multiple built-in electric fields for effectively boosting visible-light photocatalytic degradation of broad-spectrum antibiotics. Sep. Purif. Technol. 265, 118477 https://doi.org/10.1016/j.seppur.2021.118477.

Guo, M., Yuan, B., Sui, Y., et al., 2023. Rational design of molybdenum sulfide/tungsten oxide solar absorber with enhanced photocatalytic degradation toward dye wastewater purification. J. Colloid Interface Sci. 631, 33–43.

Huang, X., Guo, F., Li, M., et al., 2020. Hydrothermal synthesis of ZnSnO3 nanoparticles decorated on g-C3N4 nanosheets for accelerated photocatalytic degradation of tetracycline under the visible-light irradiation. Sep. Purif. Technol. 230, 115854.

Huang, J., Xu, X., Gu, C., et al., 2012. Size-controlled synthesis of porous ZnSnO3 cubes and their gas-sensing and photocatalysis properties. Sens. Actuators B 171–172, 572–579. https://doi.org/10.1016/j.snb.2012.05.036.

Karami, M., Ghanbari, M., Alshamsi, H.A., et al., 2021. Facile fabrication of Tl 4 HgI 6 nanostructures as novel antibacterial and antibiofilm agents and photocatalysts in the degradation of organic pollutants. Inorg. Chem. Front. 8, 2442–2460.

Konstantinou, I.K., Albanis, T.A., 2004. TiO2-assisted photocatalytic degradation of azo dyes in aqueous solution: kinetic and mechanistic investigations: a review. Appl. Catal. B: Environ. 49, 1–14.

Kumar, S.G., Rao, K.K., 2017. Comparison of modification strategies towards enhanced charge carrier separation and photocatalytic degradation activity of metal oxide semiconductors (TiO2, WO3 and ZnO). Appl. Surf. Sci. 391, 124–148.

Liu, J., Liu, N.Y., Li, H., et al., 2016. A critical study of the generality of the two step two electron pathway for water splitting by application of a C3N4/MnO2 photocatalyst. Nanoscale 8, 11956–11961. https://doi.org/10.1039/C6NR02437H.

Liu, C., Wu, L., Chen, J., et al., 2014. The nanocomposite of polyaniline and nitrogen-doped layered HTiNbO5 with excellent visible-light photocatalytic performance. PCCP 16, 13409–13417. https://doi.org/10.1039/C4CP01423E.

Lo, M.-K., Lee, S.-Y., Chang, K.-S., 2015. Study of ZnSnO3-nanowire piezophotocatalyst using two-step hydrothermal synthesis. J. Phys. Chem. C 119, 5218–5224. https://doi.org/10.1021/acs.jpcc.5b00282.

Mushtaq, M.A., Arif, M., Fang, X., et al., 2021. Photoelectrochemical reduction of N 2 to NH 3 under ambient conditions through hierarchical MoSe 2@ gC 3 N 4 heterojunctions. J. Mater. Chem. A 9, 2742–2753.

Orooji, Y., Ghanbari, M., Amiri, O., et al., 2020. Facile fabrication of silver iodide/graphitic carbon nitride nanocomposites by notable photo-catalytic performance through sunlight and antimicrobial activity. J. Hazard. Mater. 389, 122079.

Panahi, A., Ghanbari, M., Dawi, E.A., et al., 2023. Simple sonochemical synthesis, characterization of TmVO4 nanostructure in the presence of Schiff-base ligands and investigation of its potential in the removal of toxic dyes. Ultrason. Sonochem. 106362.

Paul, D.R., Gautam, S., Panchal, P., et al., 2020. ZnO-modified g-C3N4: A potential photocatalyst for environmental application. ACS Omega 5, 3828–3838. https://doi.org/10.1021/acsomega.9b02688.

Qi, C., Sun, Y., 2016. Multi-damage life assessment under continuous damage mechanics. 2016 Prognostics and System Health Management Conference (PHM-Chengdu).

Rahimzade, E., Ghanbari, M., Alshamsi, H.A., et al., 2021. Simple preparation of chitosan-coated thallium lead iodide nanostructures as a new visible-light photocatalyst in decolorization of organic contamination. J. Mol. Liq. 341, 117299 https://doi.org/10.1016/j.molliq.2021.117299.

Safajou, H., Ghanbari, M., Amiri, O., et al., 2021. Green synthesis and characterization of RGO/Cu nanocomposites as photocatalytic degradation of organic pollutants in waste-water. Int. J. Hydrogen Energy 46, 20534–20546.

Sakthivel, S., Neppolian, B., Shankar, M.V., et al., 2003. Solar photocatalytic degradation of azo dye: comparison of photocatalytic efficiency of ZnO and TiO2. Sol. Energy Mater. Sol. Cells 77, 65–82. https://doi.org/10.1016/S0927-0248(02)00255-6.

Shi, W., Guo, F., Li, M., et al., 2019. Enhanced visible-light-driven photocatalytic H2 evolution on the novel nitrogen-doped carbon dots/CuBi2O4 microrods composite. J. Alloy. Compd. 775, 511–517. https://doi.org/10.1016/j.jallcom.2018.10.095.

Spataru, N., Anastasescu, C., Radu, M.M., et al., 2018. The improvement of SiO2 nanotubes electrochemical behavior by hydrogen atmosphere thermal treatment. Appl. Surf. Sci. 444, 216–223. https://doi.org/10.1016/j.apsusc.2018.03.074.

Tahir, M.B., Nawaz, T., Nabi, G., et al., 2020. Photocatalytic degradation and hydrogen evolution using bismuth tungstate based nanocomposites under visible light irradiation. Int. J. Hydrogen Energy 45, 22833–22847.

Tang, C., Cheng, M., Lai, C., et al., 2023. Recent progress in the applications of non-metal modified graphitic carbon nitride in photocatalysis. Coord. Chem. Rev. 474, 214846 https://doi.org/10.1016/j.ccr.2022.214846.

Wang, D., Pu, X., Yu, X., et al., 2022. Controlled preparation and gas sensitive properties of two-dimensional and cubic structure ZnSnO3. J. Colloid Interface Sci. 608, 1074–1085.

Wang, D., Li, Y., Wen, L., et al., 2023. Ni-Pd-incorporated Fe3O4 yolk-shelled nanospheres as efficient magnetically recyclable catalysts for reduction of N-containing unsaturated compounds. Catalysts 13, 190.

Wang, H., Yuan, X., Wang, H., et al., 2015. One-step calcination method for synthesis of mesoporous gC 3 N 4/NiTiO 3 heterostructure photocatalyst with improved visible light photoactivity. RSC Adv. 5, 95643–95648.

Wen, L., Wang, D., Xi, J., et al., 2022. Heterometal modified Fe3O4 hollow nanospheres as efficient catalysts for organic transformations. J. Catal. 413, 779–785. https://doi.org/10.1016/j.jcat.2022.07.036.

Wenderich, K., Mul, G., 2016. Methods, mechanism, and applications of photodeposition in photocatalysis: a review. Chem. Rev. 116, 14587–14619.

Xie, K., Fang, J., Li, L., et al., 2022. Progress of graphite carbon nitride with different dimensions in the photocatalytic degradation of dyes: a review. J. Alloys Compd. 163589.

Yao, L., Wei, D., Ni, Y., et al., 2016. Surface localization of CdZnS quantum dots onto 2D g-C3N4 ultrathin microribbons: Highly efficient visible light-induced H2-generation. Nano Energy 26, 248–256. https://doi.org/10.1016/j.nanoen.2016.05.031.

Yin, Y., Shen, Y., Zhou, P., et al., 2020. Fabrication, characterization and n-propanol sensing properties of perovskite-type ZnSnO3 nanospheres based gas sensor. Appl. Surf. Sci. 509, 145335.

Zheng, Y., Yu, Z., Ou, H., et al., 2018. Black phosphorus and polymeric carbon nitride heterostructure for photoinduced molecular oxygen activation. Adv. Funct. Mater. 28, 1705407. https://doi.org/10.1002/adfm.201705407.